THE JOURNAL OF PHYSICAL CHEMISTRY B

Article

pubs.acs.org/JPCB

Molecular Simulation of Gas Solubility in Nitrile Butadiene Rubber

M. Khawaja,[†] A. P. Sutton,[†] and A. A. Mostofi*[,†,‡]

[†]Department of Physics and [‡]Department of Materials, and the Thomas Young Centre for Theory and Simulation of Materials, Imperial College London, London SW7 2AZ, U.K.

Supporting Information

ABSTRACT: Molecular simulation is used to compute the solubility of small gases in nitrile butadiene rubber (NBR) with a Widom particle-insertion technique biased by local free volume. The convergence of the method is examined as a function of the number of snapshots upon which the insertions are performed and the number of insertions per snapshot and is compared to the convergence of the unbiased Widom insertion technique. The effect of varying the definition of local free volume is also investigated. The acrylonitrile content of the polymer is altered to examine its influence on the solubility of helium, CO_2, and H_2O, and the solubilities of polar gases are found to be enhanced relative to those of nonpolar gases, in qualitative agreement with experiment. To probe this phenomenon further, the solubilities are decomposed into contributions from the neighborhoods of different atoms, using a Voronoi cell construction, and a strong bias is found for CO_2 and H_2O in particular to be situated near nitrogen sites in the elastomer. Temperature is shown to suppress the solubility of CO_2 and H_2O but to increase that of helium. Increasing pressure is found to suppress the solubility of all gases but at different rates, according to a balance between their molecular sizes and electrostatic interactions with the polymer. These results are relevant to the use of NBR seals at elevated temperatures and pressures, such as in oil and gas wells.

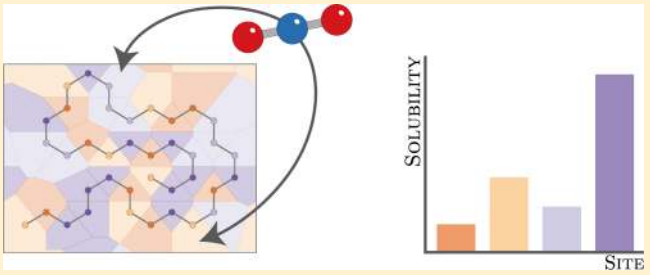

INTRODUCTION

The wide range of applications of elastomers stems from the numerous chemical compositions of the base polymer in combination with fillers and plasticizers. The former can enhance properties such as resistance to chemical attack by fuels, whereas the latter can enhance mechanical properties, such as stiffness and strength.

This diversity has led to their widespread use in sealing components, such as hoses, gaskets, O-rings, and so forth,[1] in the oil and gas industry, in which one of their key roles is to protect sensitive monitoring equipment from contamination by fluids under conditions found downhole, where temperatures and pressures can reach 225 °C and 200 MPa, respectively.[2−4] Under these conditions, two modes of permeation-driven failure are observed. The first involves the permeation of gases through the seal, leading to corrosion of the electronic components that were intended to be protected. The second occurs upon decompression, when the seals are returned to the surface too quickly, leading to a rapid pressure reduction, followed by swelling and rupture in a process known as explosive decompression.[5] This latter phenomenon is driven by the initial permeation of gases into the seal, saturating some of the voids naturally dispersed throughout the rubber,[6] followed by insufficiently rapid egress of the gases out of the seal when the external pressure is relieved.[7]

The permeation of small gases through a polymer membrane can be described by the solution−diffusion model,[8] in which the boundary conditions for diffusion through the polymer are set by the product of the solubility coefficient and the external pressures on either side of the membrane, using Henry's law.[9] Therefore, one potential option to ameliorate the decompression problem is to focus on the solubility, which inherently limits the amount of gas absorbed by the seal and sets the pressure gradient that produces the rupture. To do this, an understanding of the factors controlling solubility in the elastomer is required.

In this work, we focus on the solubility of small gases in poly(butadiene-*stat*-acrylonitrile), known as nitrile butadiene rubber (NBR) (Figure 1), widely used for sealing applications in the oil and gas industry due to its resistance to

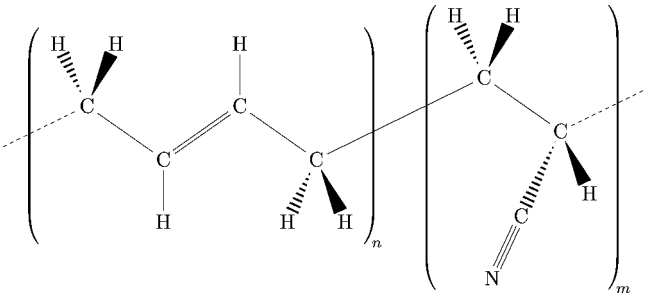

Figure 1. NBR, a statistical copolymer of butadiene (left) and acrylonitrile (ACN) (right).

Received: September 24, 2016
Revised: December 5, 2016
Published: December 6, 2016

DOI: 10.1021/acs.jpcb.6b09690
J. Phys. Chem. B 2017, 121, 287−297

hydrocarbons[10] but which under certain conditions is liable to swelling and explosive decompression.[11]

The permeability and diffusivity of small gases through NBR were characterized by Van Amerongen in the 1940s by experiment,[12,13] using a permeation cell to observe gas uptake as a function of time, obtaining the permeability from the slope and diffusivity from the time lag.[12] From the solution−diffusion model, the solubility was subsequently inferred as the quotient of the two.[8] Among the gases investigated, ranging in size from helium to methane, CO_2 was found to have the highest permeability, a fact attributed to its enhanced solubility as compared to that of smaller molecules, such as helium, which have higher diffusivities. Van Amerongen attributed this enhanced absorption to the electrostatic interaction between CO_2 and NBR. To investigate this phenomenon at a molecular level, we employ atomistic simulations to understand the factors affecting gas permeation as a function of the chemistry of the polymer and environmental conditions.

Simulating the experimental procedure used by Van Amerongen directly is impractical due to the time and length scales involved (see ref 14 for a discussion). The use of periodic boundary conditions enables the equilibrium solubilities of gases in the bulk environment of the polymer to be calculated. One method based on this approach is Widom insertion,[15] which can be used to compute the excess chemical potential of a gas dissolved in a membrane at temperature T, using an ensemble average of N separate, random, trial insertions of a solute molecule, the ith of which changes the internal energy of the system by ΔE_i

$$\mu_{ex} = -k_B T \ln\langle \exp(-\Delta E_i/k_B T)\rangle_N \quad (1)$$

where k_B is the Boltzmann constant. This quantity is defined in the dilute limit, that is, such that there are no gas−gas interactions inside the polymer, and is directly related to the solubility, s

$$s = \exp(-\mu_{ex}/k_B T) = \langle \exp(-\Delta E_i/k_B T)\rangle_N \quad (2)$$

As the polymer remains fixed, whereas the gas particles are randomly positioned, the efficacy of the Widom insertion is limited to small molecules for which polymer relaxation is unimportant.[14] Furthermore, as the insertions are performed randomly, there is a high probability of atomic overlap between the solute and host, leading to the majority of insertions contributing a negligible amount to the solubility. Therefore, care has to be taken to ensure adequate sampling, particularly at high polymer densities.

One approach to alleviate this sampling problem is to use biased insertion techniques, such as excluded volume map sampling,[16] in which regions of free volume are first identified, into which gas molecules are then inserted. This bias is then corrected for when computing the ensemble average in eqs 1 and 2 by multiplying the computed solubility by the fractional free volume.[17] As the fractional free volume is less than 10%[18] in the amorphous polymer system considered here, this can result in a speedup of at least a factor of 10, assuming that the same number of insertions per unit volume are performed. However, as insertions can take place only in the sites predetermined to be free volume, this method is inherently sensitive to the manner in which the free volume is defined.

To our knowledge, Kucukpinar and Doruker[18] are the only other authors to have investigated gas solubility in NBR through simulation. They studied the solution of small gases (the largest being methane) in NBR with 39% ACN content using a grid-based biased insertion technique and the COMPASS force field.[19] Although they were able to reproduce the ordering of solubilities found in experiment (CO_2 > O_2 > N_2 > Ne > He), precise values were generally overestimated by up to a factor of 3.4. This overestimation of solubilities (and indeed diffusivities) is found across the literature of polymer simulations[20−23] and is usually attributed to the formation of unphysically large voids in the simulation cell or the sensitivity of solubility to the force field, which is heightened by the exponential factor in eq 1. Nevertheless, simulations remain a powerful tool in predicting and explaining trends in transport properties, offering a controlled and systematic way to vary the model parameters. Some of these parameters are difficult to control in experiment, for example, replicating service conditions, whereas others are impossible to alter, for example, using hypothetical nonpolar H_2O, with the partial charges of all atoms set to zero, to determine the impact of electrostatics on the diffusion of H_2O through NBR.[18] Therefore, simulations provide insight complementary to that attainable from experiment.

In this article, we build upon our previous work on modeling bulk properties of NBR through atomistic simulation[24] to identify the key factors influencing the solubility of small gases in NBR, focusing on helium, CO_2, and H_2O, as a function of both base polymer composition and environmental conditions that reflect those found in an oil and gas exploration context. We demonstrate the importance of careful sampling of the polymer phase space when performing Widom insertion, both in terms of the size of the ensemble upon which insertions are performed and the number of insertions required for convergence. We probe the effect of increasing the ACN content in NBR, demonstrating that electrostatics is vital to the solution process in this elastomer, obtaining good agreement with the experimental trends. Using a Voronoi cell approach, the total solubilities are broken down into contributions from particular atomic environments, explicitly illustrating the preference of inserted molecules to sit near nitrogen sites in the elastomer. The temperature and pressure are varied and shown to suppress the solubility of polar solutes relative to that of nonpolar ones, suggesting that the behavior under oil and gas well conditions may be very different from that observed to date in simulations and experiments conducted under atmospheric conditions.

METHOD

NBR Model. Initially, a 1000 monomer long linear copolymer of ACN−butadiene was generated,[a] with a specified ACN content, using reactivity ratios of 0.02 and 0.28 for ACN and butadiene, respectively.[25] The copolymer was packed into a cubic simulation cell with periodic boundary conditions at a density comparable to that of experiment, 1000 kg m^{-3},[10] using a Monte Carlo method based on the self-avoiding random walk procedure of Theodorou and Suter.[26] In this approach, the backbone carbon atoms of the chain are placed at fixed distances and angles from one another but with varying dihedral angles, using the parameters from the COMPASS force field[19] and the Amorphous Cell module of BIOVIA Materials Studio v7.0. As no cross-linking was permitted, it is possible, in principle, for one starting configuration to transform into another through relaxation processes, such as reptation. However, such transformations are impossible on the time scale accessible to molecular dynamics, and in practice, the

DOI: 10.1021/acs.jpcb.6b09690
J. Phys. Chem. B 2017, 121, 287−297

Table 1. OPLS Force Field Atom Types for NBR

atom types						
element	type	mass (g mol^{-1})	σ (nm)	ϵ (kcal mol^{-1})	q (e)	note
carbon (sp^3)	CT	12.011	0.35	0.066	−0.18	C in CH_3
carbon (sp^3)	CT	12.011	0.35	0.066	−0.12	C in CH_2
carbon (sp^3)	CT	12.011	0.33	0.066	−0.02	C of CH_2 in (CH_2)−C≡N
carbon (sp^3)	CT	12.011	0.33	0.066	0.04	C of CH in (CH)−C≡N
carbon (sp^2)	CM	12.011	0.355	0.076	−0.115	C in (CH)═(CH)
carbon (sp)	CZ	12.011	0.33	0.066	0.46	C in C≡N
nitrogen	NZ	14.007	0.32	0.17	−0.56	N in C≡N
hydrogen	HC	1.008	0.25	0.03	0.06	H in $CH_{2,3}$
hydrogen	HC	1.008	0.242	0.03	0.115	H in (CH)═(CH)
hydrogen	HC	1.008	0.25	0.015	0.06	H in $(CH_{1,2})$−C≡N

starting configurations are independent. This process is repeated n = 24 times to generate an ensemble of conformations sampling the configurational phase space.

These structures were then passed into LAMMPS,[27] and the all-atom OPLS potential of Jorgensen et al.[28] was used to describe the interatomic interactions. The functional form of this force field is

$$E = \sum_{\text{bonds}} \frac{1}{2}k_r(r - r_0)^2 + \sum_{\text{angles}} \frac{1}{2}k_\theta(\theta - \theta_0)^2 + \sum_{\text{dihedrals}} \sum_{n=1}^{4} \frac{1}{2}k_{\phi n}[1 - (-1)^n \cos(n\phi)] + \sum_{i>j} 4\epsilon_{ij}f_{ij}\left[\left(\frac{\sigma_{ij}}{r_{ij}}\right)^{12} - \left(\frac{\sigma_{ij}}{r_{ij}}\right)^{6}\right] + \sum_{i>j} e^2 f_{ij}\frac{q_i q_j}{r_{ij}} \quad (3)$$

where $f_{ij} = \frac{1}{2}$ if atoms i and j are separated by three bonds, f_{ij} = 1 if they are separated by more than three bonds, and f_{ij} = 0 otherwise. Geometric combination rules are used, that is, $\sigma_{ij} = \sqrt{\sigma_{ii}\sigma_{jj}}$ and $\epsilon_{ij} = \sqrt{\epsilon_{ii}\epsilon_{jj}}$. The parameters are shown in Tables 1−4.

Table 2. OPLS Force Field Bond Types for NBR

bond types		
bonds	k_r (kcal mol^{-1} nm^{-2})	r_0 (nm)
CT−CT	53 600	0.1529
CT−CM	63 400	0.151
CT−CZ	78 000	0.147
CT−HC	68 000	0.109
CM═CM	109 800	0.134
CM−HC	68 000	0.108
CZ≡NZ	130 000	0.1157

The structures were then subjected to energy minimization (by the FIRE method[29]), compression, and relaxation (from 0.1 to 500 MPa and back to 0.1 MPa over 0.5 ns); a further energy minimization; an annealing step (from 25 to 525 °C and back to 25 °C over 1.0 ns); another cycle of compression and relaxation as before; and finally a simulation at standard ambient temperature and pressure (SATP; 25 °C and 100 kPa) for 2.0 ns. The entire equilibration procedure lasted 4 ns in total. The temperature and pressure were controlled using the Nosé−Hoover algorithm,[30] with a damping parameter of 0.1 ps for the temperature and 1 ps for the pressure.

Table 3. OPLS Force Field Angle Types for NBR

angle types		
angles	k_θ (kcal mol^{-1} rad^{-2})	θ_0 (°)
CT−CT−CT	116.7	112.7
CT−CT−CM	126	111.1
CT−CT−CZ	116.7	112.7
CT−CT−HC	75	110.7
CT−CM═CM	140	124
CT−CZ≡NZ	300	180
CT−CM−HC	70	117
CM−CT−HC	70	109.5
CM═CM−HC	70	120
CZ−CT−HC	70	108.5
HC−CT−HC	66	107.8

For configurations at elevated temperatures, the same protocol described above was used, after which the structures were heated to the required temperature at a constant rate of 10 °C ns^{-1}, followed by a 1.5 ns simulation at constant temperature and pressure.

A different approach was used to generate configurations at elevated pressures because it is not possible in molecular dynamics to simulate the reptation processes that occur in a real polymer subjected to compression. Consequently, a polymer that is compressed to a target pressure under an NPT (isothermal−isobaric) ensemble in a simulation will have a lower density than the same polymer compressed to the same pressure in experiment, leading to the solubility being systematically overestimated with respect to that from experiment. Hence, rather than attempting to simulate compression of the polymer, initial polymer configurations were directly generated at different densities using the Monte Carlo procedure described above, subjected to an energy minimization, and equilibrated in an NVT (canonical) ensemble, to maintain their densities, for a total of 4 ns. Effectively, we are using density as a surrogate variable for pressure. This can be inverted by considering the bulk modulus, B, which is related to the pressure, P, and density, ρ, at a constant mass, M

$$B = \rho\left(\frac{dP}{d\rho}\right)_M \quad (4)$$

where we have assumed that the bulk modulus is independent of pressure.[b] For most elastomers, the bulk modulus is approximately 1 GPa.[23] The solubility as a function of density can then be computed, from which the effect of pressure can be inferred.

DOI: 10.1021/acs.jpcb.6b09690
J. Phys. Chem. B 2017, 121, 287−297

Table 4. OPLS Force Field Dihedral Types for NBR

	dihedral types			
dihedrals	k_{ϕ_1} (kcal mol^{-1})	k_{ϕ_2} (kcal mol^{-1})	k_{ϕ_3} (kcal mol^{-1})	k_{ϕ_4} (kcal mol^{-1})
CT−CT−CT−CT	1.3	−0.05	0.2	0
CT−CT−CT−CM	1.3	−0.05	0.2	0
CT−CT−CT−CZ	0	0	0	0
CT−CT−CT−HC	0	0	0.3	0
CT−CT−CM═CM	0.346	0.405	−0.904	0
CT−CT−CM−HC	0	0	0	0
CT−CT−CZ≡NZ	0	0	0	0
CT−CM═−CM−CT	0	14	0	0
CT−CM═CM−HC	0	14	0	0
CM−CT−CT−CM	0	0	0	0
CM−CT−CT−CZ	0	0	0	0
CM−CT−CT−HC	0	0	0.366	0
CM═CM−CT−HC	0	0	−0.372	0
CZ−CT−CT−HC	0	0	0.366	0
NZ−CZ−CT≡HC	0	0	0	0
HC−CT−CT−HC	0	0	0.3	0
HC−CT−CM−HC	0	0	0.318	0
HC−CM═CM−HC	0	14	0	0

Table 5. Nonbonded Parameters, Bond Lengths, and Angles for Gases Used for Widom Insertion

molecule	atom	σ (Å)	ϵ (kcal mol^{-1})	q (e)	r_0 (Å)	θ_0 (°)	source
He	He	2.556	0.02	0.0			OPLS[28]
CO_2	C	2.757	0.0559	0.6512	r_{CO} = 1.149	θ_{OCO} = 180	EPM2[34]
	O	3.033	0.16	−0.3256			
H_2O	H	0.0	0.0	0.41	r_{HO} = 1.0	θ_{HOH} = 109.47	SPC[33]
	O	3.166	0.1554	−0.82			

Each equilibrated structure was then evolved dynamically, and m = 250 snapshots were taken for each, one every 25 ps for 6.25 ns, to improve sampling for the calculation of solubility. The fastest vibrational modes in the system (the C−H bonds) were always constrained using the SHAKE algorithm[31] to enable a time step of 2.5 fs to be used, except during annealing steps in the equilibration protocol, during which no constraints were applied and a 1 fs time step was used.

This model for NBR was validated in our previous work[24] by comparing predicted bulk properties, such as density and glass-transition temperature, as a function of ACN content to experimental data. The densities were found to agree with the experimental values to within 5%, and the experimentally observed trend of an increasing glass-transition temperature with ACN content was reproduced.[10]

Solubility. *Overview.* Solubilities were computed by performing Widom insertion[15] using Gromacs[32] and its "Test Particle Insertion" routine. Random (unbiased) insertions and insertions biased by the free volume were performed.

Parameters for helium were taken from the OPLS force field,[28] whereas H_2O and CO_2 were described using the SPC[33] and EPM2[34] force fields, respectively. Although many alternative potentials exist in the literature, particularly for H_2O and CO_2, we chose to use physically reasonable atomistic descriptions and then focus on investigating qualitative trends, rather than to seek precise quantitative agreement with experiment, something that solubility simulations in polymers often find difficult to do.[14] The parameters for the inserted molecules are provided in Table 5.

For all simulations performed in the NPT ensemble, the excess chemical potential given in eq 1 is corrected for volume fluctuations[35]

$$\mu_{ex} = -k_B T \ln \frac{\langle V_i \exp(-\Delta E_i/k_B T)\rangle_N}{\langle V_i\rangle_N} \quad (5)$$

where V_i is the instantaneous volume of the simulation cell. This correction is typically small, as the standard deviation in the cell volumes of the equilibrated structures is less than 0.5%.

Unbiased Widom Insertion. N insertions are performed at random positions and, if applicable, with random molecular orientations, within a snapshot of the polymer generated from molecular dynamics. No relaxation is performed to accommodate the inserted species. The change in the total potential energy, ΔE_i, upon insertion is calculated, the Boltzmann factor is calculated, and these factors are averaged to obtain the solubility according to eqs 1, 2, and 5.

The implementation of this method in Gromacs proceeds as follows: for a given snapshot of a frozen polymer, an initial insertion position is randomly chosen anywhere inside the simulation cell, the atom or molecule is inserted, it is treated as a rigid body and rotated if possible, and the initial neighbor list and long-range electrostatic energies are computed. Then, the remaining short-range terms in the energy are also calculated, to yield ΔE_i. For the next $a - 1$ insertions (where a is a user-defined parameter), the gas molecule is shifted randomly about its initial position within a sphere of radius r (and a further random rotation is applied if applicable), whose value is small, such that the neighbor list and long-range electrostatic energies can be assumed to remain unchanged, before the other terms in the energy are computed, to obtain ΔE_i at each step. A new

DOI: 10.1021/acs.jpcb.6b09690
J. Phys. Chem. B 2017, 121, 287−297

initial position is then chosen randomly in the box, and this process is repeated until N insertions in total have been performed. The insertions are subsequently computationally inexpensive and easily parallelizable.[c] The parameters a and r were set to 10 and 0.05 nm, respectively.

To obtain solubilities within a standard error of 5%, $N = 10^8$ insertions are required for all gas molecules, with the exception of helium, for which $N = 10^6$ insertions are found to be sufficient, on $m = 250$ equilibrated snapshots from each of $n = 24$ independent configurations generated with the Monte Carlo procedure described earlier.

Biased Widom Insertion. As insertions into regions already occupied by atoms contribute a negligible amount to the solubility, biased insertions are performed only where there is free volume. A map of the free volume is defined for a given snapshot, insertions are performed at random positions (and orientations) within such regions, and the total solubility is calculated after accounting for the bias that has been introduced.

To generate a map of the free volume, the cubic simulation cell is divided into a cubic grid of $N_{grid} = 10^6$ points, with a helium probe atom placed at each grid point. Using the distance, r_{ij}, from a probe at point i to polymer atom j, the number density at that point, f_i, is computed in terms of distance δ_{ij}

$$f_i = \sum_{j=1}^{N_{atoms}} H(\delta_{ij}) \tag{6}$$

$$\delta_{ij} = (1 - \alpha)\sqrt{\sigma_{He}\sigma_j} - |r_{ij}| \tag{7}$$

where H is the Heaviside step function, σ_{He} and σ_j are the Lennard-Jones widths of the helium probe and polymer atom, respectively, α is a free parameter used to tune the definition of the free volume, and summation is performed over N_{atoms} of the polymer.[d] The free-volume sites are defined as those for which $f_i = 0$.

The set of free-volume sites for a given snapshot is then passed into a modified version of Gromacs' particle-insertion routine, `tpi.c`, in which insertions are performed in each of the voxels centered on the grid points. As they are small, no larger than 0.1 nm, it is assumed that the neighbor list and long-range electrostatic energy remain unchanged within a given voxel; therefore, additional positions and orientations after the first one may be sampled while only recomputing the short-range terms in the energy. The effect of changing the number of insertions per grid point is examined in the Results and Discussion section, and the sensitivity of solubility to the free volume is examined in the Supporting Information. The final values chosen are $\alpha = 0.2$, $N_{grid} = 10^6$, and 100 insertions per grid point defined as free volume. For a fractional free volume of 1%, this corresponds to 10^6 insertions in total, 100 times fewer than that in the full Widom insertion method. Although it takes time to generate a free-volume map, this is required only once per snapshot, as it is independent of the molecule being inserted and ultimately the speedup is close to a factor of 100.[e]

The bias introduced by sampling insertions only in regions of free volume is accounted for by multiplying the solubility by the probability of insertion in free volume, that is, the fractional free volume

$$s = \frac{N_{fv}}{N_{grid}} \exp(-\mu_{ex}/k_B T) \tag{8}$$

where N_{fv} is the number of free-volume sites, that is, those where $f_i = 0$.

Localized Solubility. To identify the atomic environments in NBR in which polar gases have lower energies, the total solubility of each gas in NBR of a fixed ACN content (41.3%) at SATP was decomposed into contributions according to the type of atom in the polymer closest to the inserted molecule. Voronoi cells were constructed around each atomic site of the polymer, ignoring hydrogen atoms, using the Voro++ library,[36] and unbiased Widom insertions were sorted into the Voronoi cells according to the positions of the centers of mass of the inserted molecules, together with the corresponding Boltzmann factors. Sorted insertions belonging to atoms of the same orbital hybridization state, sp^1, sp^2, sp^3 carbons and nitrogen, are grouped, and the Boltzmann factors are summed and normalized by the total Boltzmann factor across all groups so that the relative contribution of different atomic sites can be compared across different inserted molecules and the solubilities per group sum to the total solubility.

Owing to the demands on processor, memory, and storage of writing and sorting, of the $N = 10^8$ insertions performed on up to $n \times m = 24 \times 250 = 6000$ configurations, most of which contribute a negligible amount to the solubility, only a subset of insertions whose insertion energies were less than $5k_BT$ ($T = 25$ °C) were used. For CO_2, this approach reduced the number of insertions written per snapshot from 10^8 to approximately 8×10^4, that is, a factor of 1000 fewer insertions to process, while maintaining the precision of the solubility at better than one part in 10^6 as compared to that on using all insertions.

Errors. Standard Error. When determining the standard error, it would be incorrect to treat all $n \times m$ snapshots as independent, as snapshots generated from the same starting configuration will be correlated with one another because the relaxation time of the polymer exceeds the duration of the simulations. Instead, for initial configuration i, where $i = 1, 2, ..., n$, the solubilities, s_{ij}, computed for m snapshots, where $j = 1, 2, ..., m$, are used to calculate an average solubility, s_i. The set of values of s_i is then averaged over the n independent starting configurations to obtain $\bar{s}$, and the standard error, SE, may be calculated using the standard deviation, σ, of the n values of s_i

$$s_i = \frac{1}{m}\sum_{j=1}^{m} s_{ij} \tag{9}$$

$$\bar{s} = \frac{1}{n}\sum_{i=1}^{n} s_i \tag{10}$$

$$\sigma^2 = \frac{1}{n}\sum_{i=1}^{n} (s_i - \bar{s})^2 \tag{11}$$

$$\mathrm{SE} = \frac{\sigma}{\sqrt{n}} \tag{12}$$

The standard error in the solubility is reduced using n independent starting configurations because the spread in the average solubilities, s_i, for each starting configuration is smaller.

Resampling. The convergence of the standard error in the solubility with n, SE(n), becomes poor when n is small. For example, the standard error for $n = 2$ depends on which two initial configurations are chosen. These fluctuations eventually become negligible for a sufficiently large n. Randomized subsampling can be used to dampen the fluctuations,[37−39] by sampling subsets of data, computing the statistical quantity of

DOI: 10.1021/acs.jpcb.6b09690
J. Phys. Chem. B 2017, 121, 287−297

interest for each subset, and averaging all quantities. This enables the computation of, for example, the average standard error as a function of the number of independent configurations, $\overline{\mathrm{SE}}(a)$, which is useful for determining how many configurations are needed to obtain the solubility to within a desired level of precision. The method to compute $\overline{\mathrm{SE}}(a)$ is as follows: given n average solubilities in total, randomly select a of them, compute the standard error as previously described over the a solubilities, and repeat this process until $\overline{\mathrm{SE}}(a)$ has converged (10^3 attempts were found to be sufficient).

RESULTS AND DISCUSSION

Convergence. First, we present a study of the convergence of the solubilities computed with the unbiased and biased Widom insertion techniques with respect to the number of independent initial configurations, n; the number of snapshots, m, taken from molecular dynamics simulations after equilibrating each initial configuration; and the number of insertions per snapshot, N. We justify the choice of $n = 24$ and $m = 250$ on the basis of the convergence of the standard error in the solubility of CO_2, and the significant inhomogeneity of CO_2 insertions for small n and m is discussed in the Supporting Information. Then, we justify the choice of $N = 10^8$ for the unbiased Widom insertion technique and highlight the advantages that biased insertion offers over unbiased insertion by reducing N for the same precision in the solubility.

For biased Widom insertions, the sensitivity of the solubility to the free volume is discussed in the Supporting Information in terms of the number of grid points and the free-volume tuning parameter, α, set at 10^6 and 0.2, respectively. All convergence simulations are performed at SATP for NBR of 41.3% ACN content.

Number of Starting Configurations, n, and Number of Snapshots for Each, m. Figure 2 shows the standard error in the solubility of CO_2 as a percentage of its average solubility, as a function of n and m for the unbiased and biased Widom insertion techniques. Random resampling is performed using 10^3 steps to smooth out the fluctuations that would otherwise arise for small n. Increasing n brings about the most rapid reduction in the standard error. However, this has to be balanced against computational cost because equilibrating an independent configuration requires a 4 ns simulation, whereas generating an additional snapshot takes only 25 ps. Balancing these considerations while minimizing the standard error in solubility led to the choice of $n = 24$ and $m = 250$. The convergence is almost identical for unbiased and biased Widom insertion techniques.

Number of Insertions. Figure 3 shows the convergence of the solubility of CO_2 as a function of the number of insertions, for both the unbiased and biased Widom insertion techniques. For the former, 10^{10} insertions were performed on each snapshot, corresponding to a sampling density of approximately 10^8 nm^{-3}, and this defined the limiting solubility, s_{lim}. A subset, N, of these insertions were randomly selected and averaged to obtain solubility s_N, and the relative root-mean-squared deviation of s_N from s_{lim} was computed, that is, $|s_N - s_{\mathrm{lim}}|/s_{\mathrm{lim}}$. Because of the noise in the data, random resampling was performed as described earlier. This procedure was repeated over a single snapshot generated from each of $n = 24$ independent configurations, and the fractional error was averaged as a function of the number of insertions. With

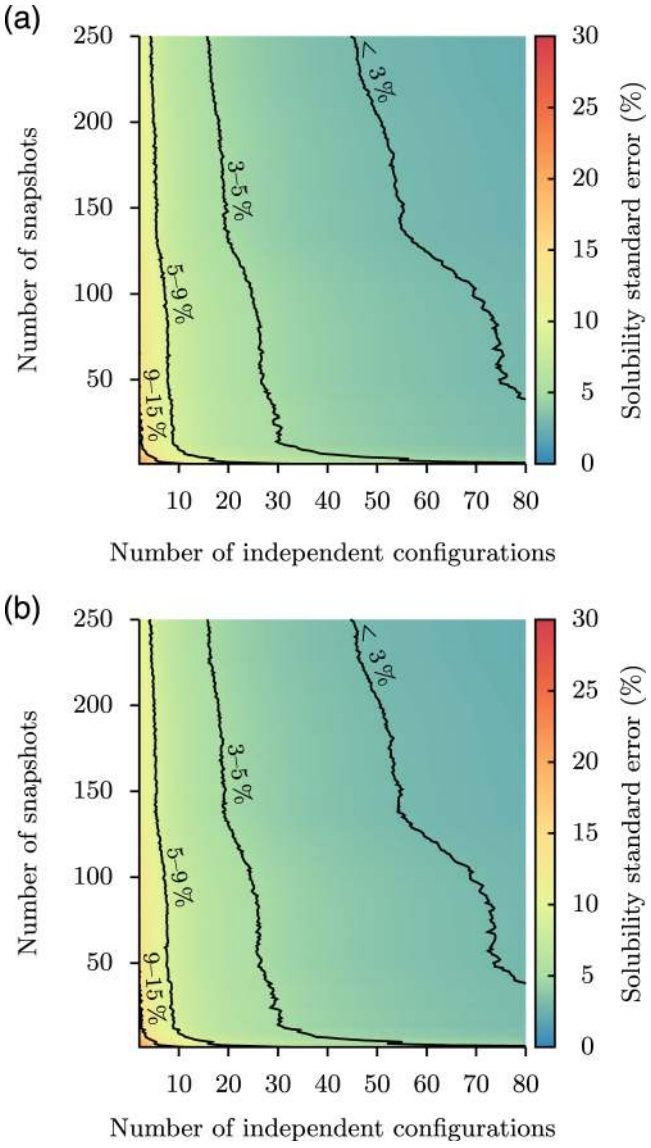

Figure 2. Convergence of CO_2 solubility with the number of independently generated configurations and number of dynamically evolved snapshots, in terms of the standard error as a percentage of the solubility, for (a) unbiased Widom insertions and (b) biased Widom insertions. The unbiased Widom insertion technique uses 10^8 insertions per snapshot. The biased Widom insertion technique uses 10^6 grid points, 100 insertions per grid point identified as free volume, and $\alpha = 0.2$, corresponding to an average of 2.55×10^6 insertions per snapshot, that is, a speedup of a factor of almost 40 compared to that for the unbiased Widom insertion technique.

every increase in the number of insertions, the difference in the fractional error drops, suggesting that it is asymptotically approaching the $N \rightarrow \infty$ solubility limit. In practice, it was found that using 10^8 insertions over $n \times m = 24 \times 250 = 6000$ snapshots was sufficient to ensure a standard error in the solubility of no more than 5%.

For biased Widom insertion, the approach to calculating s_{lim} is similar except that the total number of insertions is not a user-definable parameter, as it depends on the fractional free volume of the system. Instead, we define the number of grid points (10^6) and number of insertions per grid point (10^4), and the total number of insertions is then inferred as the fractional free volume times the product of these two quantities. The

DOI: 10.1021/acs.jpcb.6b09690
J. Phys. Chem. B 2017, 121, 287−297

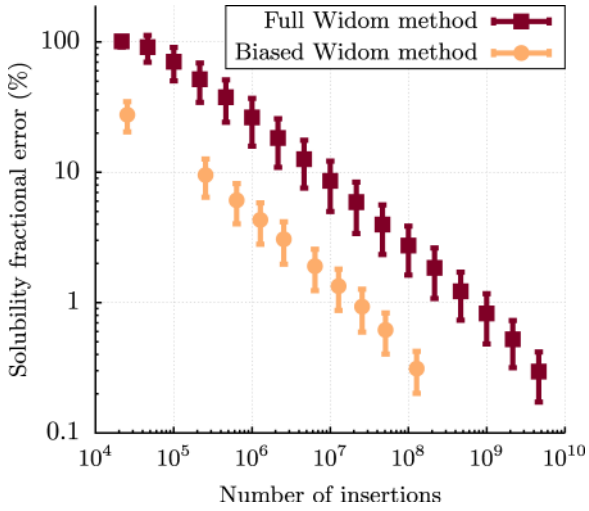

Figure 3. Convergence of CO_2 solubility with the number of insertions is shown for both the unbiased and biased Widom insertion techniques, in terms of the fractional error of the solubility, $|s_N - s_{lim}|/s_{lim}$, where s_N is the solubility after N insertions. For the unbiased Widom insertion technique, s_{lim} corresponds to the solubility after a total of 10^{10} insertions. For the biased Widom insertion technique, s_{lim} corresponds to the solubility obtained after performing 10^4 insertions per grid point defined as free volume. The number of grid points is 10^6, the free-volume tuning parameter, α, is 0.2 (see eq 7), and the average fractional free volume is (2.55 ± 0.07)%. The fractional error is averaged over one snapshot obtained from each of 24 initial configurations. The error bars represent the standard deviation in the fractional error.

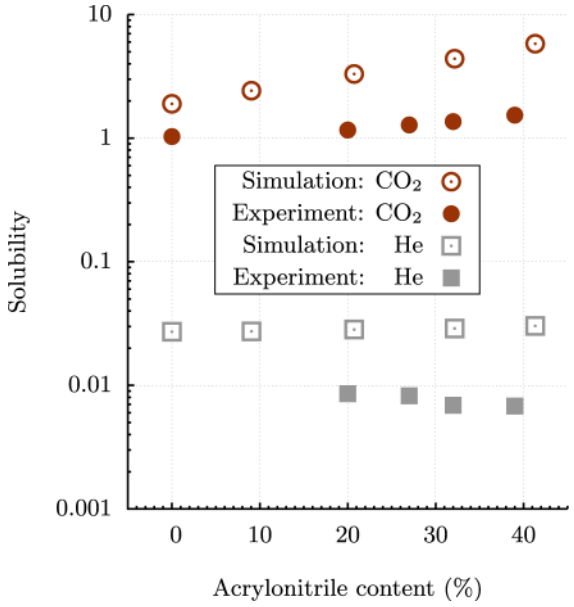

Figure 4. Solubility of helium and CO_2 as a function of ACN content from simulation and experiment. Experimental data from Van Amerongen[12,13] for NBR at SATP. Insertions were performed using the biased Widom insertion technique, with 100 insertions per grid point identified as free volume, 10^6 grid points, and α = 0.2. NBR snapshots were generated at SATP.

biased Widom insertion technique converges significantly faster than the unbiased Widom insertion technique, reaching a fractional error of less than 5% with approximately 100 times fewer insertions, corresponding to 50 insertions per grid point. To account for possible variations between different inserted molecular species and NBR of differing ACN contents, a conservative value of 100 insertions per grid point was chosen.

Solubility under Standard Conditions. When studying the permeation of small gas molecules through NBR, Van Amerongen[12] found that CO_2 demonstrated a higher gas permeability compared to that of nonpolar gases, due to its higher solubility. For example, the permeability of CO_2 in NBR (32% ACN content) is almost double that of helium, despite its diffusivity being approximately an order of magnitude smaller. Here, we seek a quantitative understanding of the enhanced solubility of CO_2.

One of the main parameters that may be varied when creating a commercial formulation of NBR is the ACN content. As the ACN content is increased, the glass-transition temperature of the polymer increases, it becomes stiffer, and its resistance to swelling from fuels improves.[10]

In Figure 4, our computed solubilities for CO_2 and helium as a function of ACN content are compared to the limited experimental data available, taken from Van Amerongen.[12,13] Consistent with other Widom insertion simulations in the polymer literature,[14] the solubilities are overestimated with respect to experiment by a factor of between 2 and 5.

Despite the comprehensive convergence tests performed in this work, it is not possible to rule out the possibility of sampling issues in these simulations. It may be the case that in reality the length scale over which the polymer is homogeneous is longer than the typical dimensions of a molecular simulation, for example, due to the presence of submicroscopic voids.[6]

Another factor is the force field, to which the solubility is sensitive as a result of the exponential dependence on energy, shown in eqs 1 and 2. The nonbonded parameters in force fields, such as OPLS, are parameterized using bulk static properties, such as density and heat of vaporization,[28] and it is unlikely that this will ensure correct treatment of properties dependent on local atomic environments, such as solubility of gases and transport properties.

Nevertheless the experimental trends with ACN content are reproduced. In particular, the solubility of CO_2 is found to be higher than that of helium, despite CO_2 being larger. This could be attributed to electrostatics, as CO_2 is a quadrupolar molecule, but it may also be related to van der Waals effects, as Lennard-Jones interactions are both stronger and longer-ranged for CO_2. To investigate the contribution of electrostatics, the solubility of nonpolar CO_2, that is, with its partial charges set to zero, was studied and compared to the solubility of normal CO_2, helium, H_2O, and nonpolar H_2O (Figure 5).

The solubilities of all gases increased with increasing ACN content, but the increase is most pronounced with polar gases. This suggests that electrostatic interactions between the ACN monomer and the molecules are responsible for this trend, which seems reasonable given that the ACN monomer contains the largest dipole in the polymer, in the C≡N functional group, and H_2O and CO_2 contain a dipole and quadrupole, respectively.

The nonpolar CO_2 and H_2O molecules exhibit higher solubilities than helium, suggesting that the stronger and longer-ranged van der Waals interactions in these molecules are able to overcome their larger molecular volumes. Indeed, this also appears to be the case for nonpolar CO_2 versus nonpolar H_2O, as CO_2 has the higher solubility despite being larger (nonpolar SPC H_2O is effectively just an oxygen atom,[f] as the

DOI: 10.1021/acs.jpcb.6b09690
J. Phys. Chem. B 2017, 121, 287−297

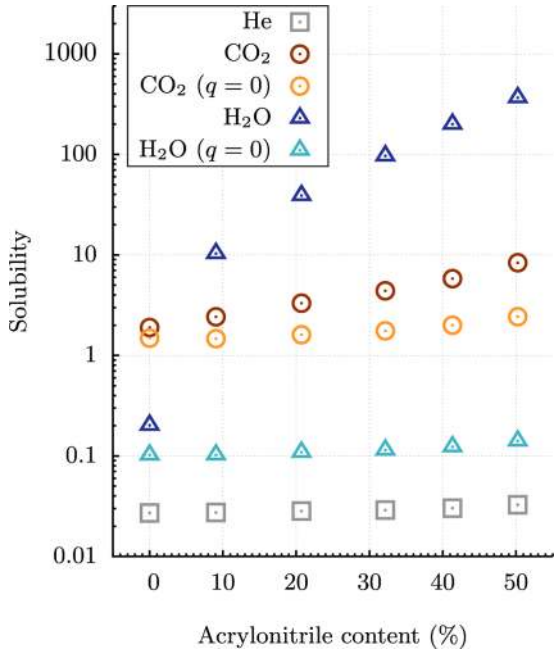

Figure 5. Calculated solubilities of CO_2, H_2O, and helium as a function of ACN content. For CO_2 and H_2O, the solubilities are also shown for the cases in which the atomic charges are turned off ($q = 0$). Insertions were performed using the biased Widom insertion technique, with 100 insertions per grid point identified as free volume, 10^6 grid points, and $\alpha = 0.2$. NBR snapshots were generated at SATP.

hydrogen atoms are only virtual charge sites with zero Lennard-Jones interactions).

It is perhaps surprising that the solubility increases even though the density of NBR is known to increase with ACN content both in experiment[40] and in simulation.[24] However, in our simulations, the total free volume increases with ACN content as well, by approximately 11%, when going from 0% ACN (i.e., amorphous polybutadiene) to 50.2% ACN NBR. This could be attributed to the increasing number of side chains in the system, randomly distributed along the chain, hindering efficient packing of the polymer and therefore increasing the available volume for insertions, the number of successful insertions, and the solubility.

To investigate further the reasons for the increasing solubility with ACN content, a break-down of the total solubility of various gases in NBR into localized contributions from each atom type in the polymer (excluding hydrogen), where the hybridization states of carbon atoms are distinguished, is shown in Figure 6. The fractional volume associated with each atomic environment is calculated using the Voronoi cell construction described earlier and is also shown in Figure 6. Given that there is only one nitrogen atom per ACN monomer, it is unsurprising that nitrogen and the sp-carbon that it is bonded to take up the least volume in the system. However, despite this, a disproportionate fraction of the solubility of all gases comes from insertions that fall closest to nitrogen atoms. This is especially noticeable for gases with electrostatic interactions, such as CO_2 and H_2O, with almost all of the solubility of water being attributed to nitrogen environments.

For helium, as the interactions with the polymer are almost entirely repulsive (ϵ = 0.02 kcal mol^{-1}), its distribution of solubilities will effectively be the same as that for a hard sphere, that is, it will largely reflect the free volume in the system. Other gases with no electrostatic interactions with the polymer exhibit similar distributions in their solubilities to those of helium.

Solubility at Elevated Temperature and Density. *Temperature.* As shown in Figure 7, raising the temperature affects the solubility of different gas species in different ways, suppressing the solubility of CO_2, nonpolar CO_2, and H_2O but enhancing that of helium and nonpolar H_2O. The computed and experimental[12,13] solubilities for CO_2 and helium are also compared, showing that our simulations on CO_2 agree with the trend found in experiment; however, the slight increase in the solubility of helium between 25 and 50 °C found experimentally seems to be too subtle to be seen in our simulations.

Density. As reported widely in the literature, care has to be taken when performing any type of Widom insertion on dense systems when fewer attempted insertions are successful, owing to the increased probability of atomic overlap between the solute and host. The CO_2 convergence tests performed at atmospheric pressure and 25 °C were repeated at two higher densities to test the effect of independently varying the free-volume tuning parameter, α, from 0.2 to 0.5; the number of

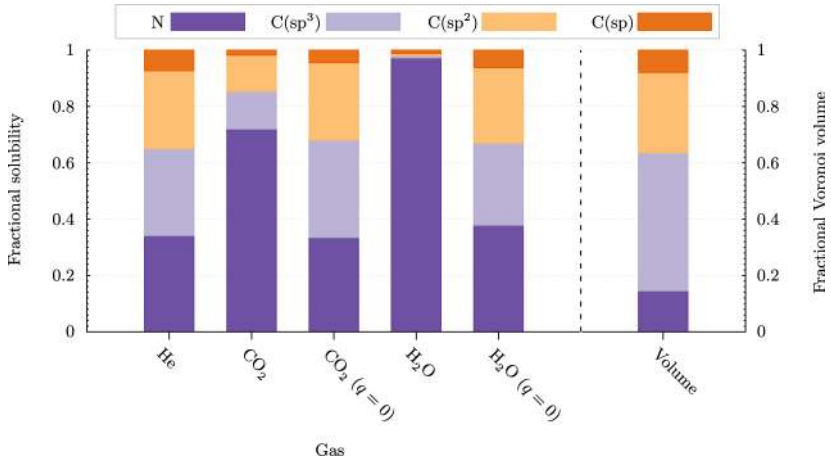

Figure 6. Total solubility for each gas decomposed into fractional contributions according to the atomic environment in which the gas is located. The fractional volumes associated with each atomic environment are shown on the right for comparison. Insertions were performed using the unbiased Widom insertion technique, with $N = 10^8$. NBR of 41.3% ACN content was generated at SATP.

DOI: 10.1021/acs.jpcb.6b09690
J. Phys. Chem. B 2017, 121, 287−297

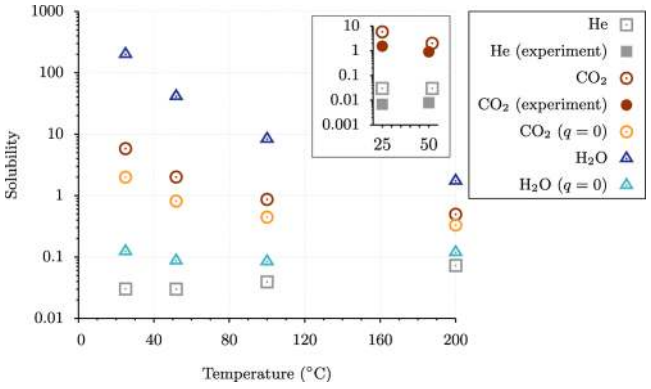

Figure 7. Solubilities of various gases in NBR as a function of temperature. Inset: comparison of simulated and experimental solubilities for CO_2 and helium. Simulations were performed at standard pressure for NBR of 41.3% ACN content. Insertions were performed using the biased Widom insertion technique, with 100 insertions per grid point defined as free volume, 10^6 grid points, and α = 0.2. Experimental data are from Van Amerongen[12,13] for NBR of 39% ACN.

grid points per dimension, $N_{\text{grid}}^{1/3}$, from 100 to 400; and the number of insertions per grid point from 100 to 2000. For ρ = 1200 kg m^{-3} ($P \approx \frac{1}{4}B = 250$ MPa), it was found that in all cases the average solubility was within 5% of the original value of 0.027. For ρ = 1440 kg m^{-3} ($P \approx \frac{1}{2}B = 500$ MPa), the solubility was within an order of magnitude of the original value of 10^{-15}, that is, effectively zero. Therefore, we returned to using the original parameters.

The solubility as a function of density is shown in Figure 8, in which the density of NBR at SATP in the simulation is $\rho \approx 960$ kg m^{-3}.[24] Although all gases exhibit a decrease in their solubilities with increasing density, the rates at which they decrease vary. As the larger of the two molecules, the solubility of CO_2 falls below that of helium at a density of 1250 kg m^{-3}, equating to a pressure of approximately 300 MPa. Given their behavior with increasing temperature, shown in Figure 7, this crossover point should occur even sooner if both the temperature and pressure are raised concurrently, as they might be in an oil and gas drilling context. This is demonstrated by Figure 8b, which shows the solubility as a function of pressure at 200 °C, resulting in a crossover density of approximately 1025 kg m^{-3}.

The solubility of H_2O at 25 °C reaches 0 at a density of 1600 kg m^{-3} or pressure of approximately 670 MPa, far beyond the conditions found in oil and gas wells, in which, typically, pressures reach 200 MPa and temperatures reach 225 °C.[2−4] This can be attributed to the virtual charges present in the SPC model of water on the hydrogen sites and the lack of any Lennard-Jones repulsion from these sites, with overlap being prevented largely by the central oxygen atom. The electrostatic attraction from the virtual charges appears to overcome the Lennard-Jones repulsion up to large densities. This is supported by the observation that the solubility of H_2O without any partial charges is significantly lower. Electrostatics does not seem to be as big a factor for CO_2, suggesting that steric effects dominate in this case.

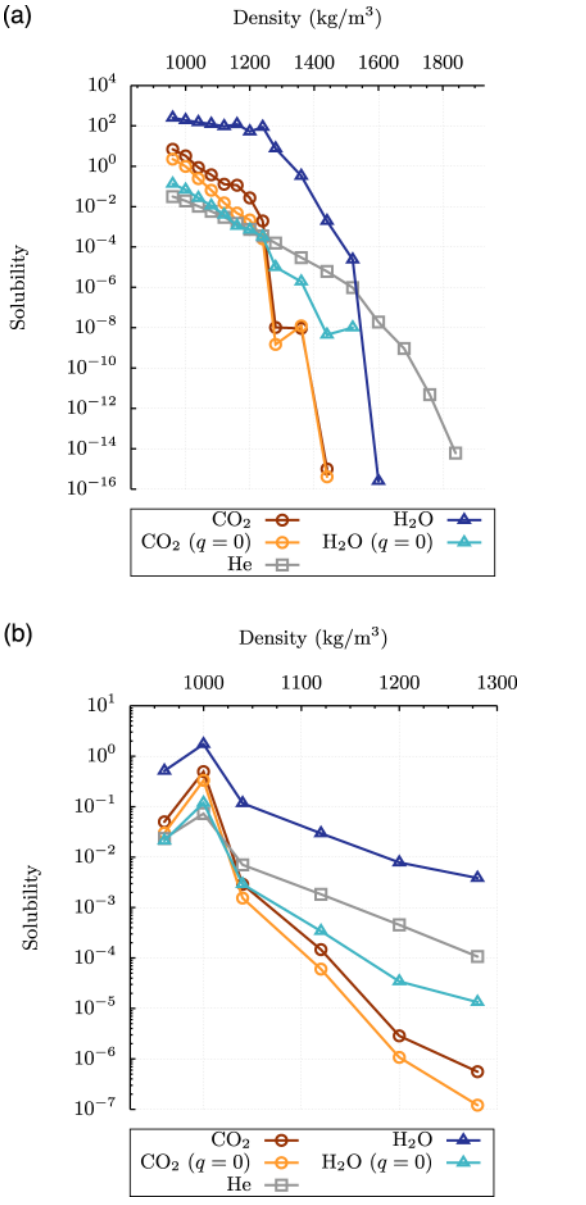

Figure 8. Solubilities of various gases as a function of density. Lines are shown to guide the eye and are terminated when the solubility reaches 0 or the density reaches 1840 kg m^{-3}, whichever comes first. Simulations were performed for NBR of 41.3% ACN content at (a) 25 °C and (b) 200 °C. Insertions were performed using the biased Widom insertion technique, with 100 insertions per grid point defined as free volume, 10^6 grid points, and α = 0.2.

CONCLUSIONS

In this work, molecular simulation was used to investigate the solubilities of small molecules in NBR. The need for careful sampling when performing Widom insertion was demonstrated for insertions performed randomly using the unbiased Widom insertion technique as well as those performed in regions of free volume using the biased Widom insertion technique. Following examination of the various parameters, it was found that the biased Widom insertion technique provides a minimum speedup of a factor of 40 when compared with the unbiased Widom insertion technique, with no loss of precision in the calculated solubility to within the 5% standard error found in both cases. These sampling tests were repeated in two systems at higher pressures (approximately 250 and 500 MPa) to

DOI: 10.1021/acs.jpcb.6b09690
J. Phys. Chem. B 2017, 121, 287−297

ensure that convergence was maintained in cases in which fewer successful insertions contribute to the solubility. No significant change in the solubility was observed.

As a copolymer of ACN and butadiene, the monomer composition of NBR is often varied in industrial applications, e.g., increasing the ACN content to increase mechanical stiffness. Gaining an understanding of how the density of the polymer and solubilities of different gases are affected by these changes is of interest. The bulk properties of NBR (and HNBR), such as density and glass-transition temperature, were investigated using simulations in our previous work,[24] whereas the permeability of a few gases as a function of the ACN content was studied experimentally in the 1940s by Van Amerongen.[12,13]

In this work, we utilized molecular simulations to understand the possible causes of some of the trends observed in experiment. The effect of varying the ACN content was studied, and the trends of increasing solubility of CO_2 and helium were reproduced, in qualitative agreement with experiment, whereas H_2O, for which no experimental data were available for comparison, demonstrated the highest solubility of all, owing to its dipole moment. Precise values of the solubilities were systematically overestimated by a factor of 2−5, consistent with other Widom insertion simulations in the literature,[14] a result often attributed to a combination of length-scale issues, for example, the presence of voids in the real polymer that are on a length scale larger than that studied in a typical molecular simulation and deficiencies in the force field, which the solubility is sensitive to.

To probe the enhanced absorption of polar gases in NBR, solubilities were computed according to the local atomic environment of the sites selected by the gases. It was found that nonpolar gases followed a similar pattern, mirroring fairly closely the free-volume distribution. Polar gases showed a clear bias toward being situated near the nitrogen sites of the elastomer, suggesting that electrostatics is the key reason for their enhanced solubilities.

As NBR is commonly used in elastomer seals that are subjected to high pressures and temperatures, for example, in an oil and gas exploration context, the solubility of gases in NBR at elevated temperatures and densities was examined. It was found that raising the temperature affected different gases in different ways, increasing the solubility of helium but suppressing that of H_2O and CO_2. Increasing the density reduced the solubility of all gases; however, it did so at different rates, with the solubility of CO_2, for example, dropping below that of helium but at densities far exceeding those an elastomer might reach in an oil and gas context. Our results further showed that if both the temperature and pressure were raised concurrently, as they typically would in an industrial setting, this crossover would occur even sooner.

This work is a first step toward understanding the trends in the solubility of small gases in NBR through molecular simulations. As the cyano group was shown to be a vital contributor to the enhanced solubility of polar gases, it is evidently a potential candidate for chemical modification to reduce the costly problems of elastomer seal swelling and explosive decompression.

The source code and data underlying this article, including the initial structures in the LAMMPS format, LAMMPS equilibration files, the free-volume analysis code, and the modified GROMACS particle-insertion code, are available through figshare[41] and can be used under the Creative Commons Attribution license. Copies of references that do not have permanent digital object identifiers are available on request from the corresponding author.

■ ASSOCIATED CONTENT

Supporting Information

The Supporting Information is available free of charge on the ACS Publications website at DOI: 10.1021/acs.jpcb.6b09690.

Inhomogeneity of particle insertions and sensitivity of solubility to the definition of free volume (PDF)

■ AUTHOR INFORMATION

Corresponding Author

*E-mail: a.mostofi@imperial.ac.uk. Phone: +44 (0)20 7594 8154.

ORCID

M. Khawaja: 0000-0002-1620-3879

Notes

The authors declare no competing financial interest.

■ ACKNOWLEDGMENTS

The authors acknowledge support from the Thomas Young Centre under grant TYC-101; M.K. was supported through a studentship in the Centre for Doctoral Training on Theory and Simulation of Materials at Imperial College London, funded by EPSRC under Grant No. EP/G036888/1 and by Baker Hughes Inc. Via our membership of U.K.'s HEC Materials Chemistry Consortium, which is funded by EPSRC (EP/L000202), this work used the ARCHER U.K. National Supercomputing Service (http://www.archer.ac.uk). Thanks to John Stevens, Jimmy Eason, and David Curry from Baker Hughes Inc. and to Imperial College London High-Performance Computing Facility.

■ ADDITIONAL NOTES

[a]The degree of polymerization of NBR in experiment is 400−20 000.[10]

[b]Although in practice the pressure−volume curve fits a Birch−Murnaghan relationship, the nonlinearity is not too severe, especially at low pressures, and therefore this is a reasonable assumption.

[c]For example, we are able to run 10^8 insertions on a 8763 atom system in under 6 min on 16 cores using two Intel Xeon E5-2640 v2 processors on a dual-socket motherboard.

[d]In practice, the sum is terminated as soon as a nonzero term is found, as we are only interested in the free volume and not the precise number density of the excluded volume.

[e]Without using any optimization techniques, such as constructing cell lists to limit the domain of potential atomic neighbors, the free-volume map generation over 10^6 grid points takes only 30 s on a single core.

[f]Albeit one with a slightly larger σ than that usually utilized for oxygen.

■ REFERENCES

(1) Ciesielski, A. *Introduction to Rubber Technology*; Rapra Technology Limited, 1999; Vol. 44.

(2) Lake, L. W.; Mitchell, R. F. *Petroleum Engineering Handbook: Drilling Engineering*; Society of Petroleum Engineers, 2006; Vol. 2.

(3) Avant, C.; Daungkaew, S.; Behera, B.; Danpanich, S.; Laprabang, W.; del Santo, I.; Heath, G.; Osman, K.; Khan, Z.; Russel, J.; et al.

DOI: 10.1021/acs.jpcb.6b09690
J. Phys. Chem. B 2017, 121, 287−297

Testing the Limits in Extreme Well Conditions. *Oilfield Rev.* **2012**, *24*, 4−19.
(4) Baker Hughes, 2013 Annual Report. http://phx.corporate-ir.net/phoenix.zhtml?c=79687&p=irol-reportsannual (accessed Sept 2016).
(5) Briscoe, B.; Savvas, T.; Kelly, C. "Explosive Decompression Failure" of Rubbers: A Review of the Origins of Pneumatic Stress Induced Rupture in Elastomers. *Rubber Chem. Technol.* **1994**, *67*, 384−416.
(6) Gent, A. N. Nucleation and Growth of Gas Bubbles in Elastomers. *J. Appl. Phys.* **1969**, *40*, 2520.
(7) Stevenson, A.; Morgan, G. Fracture of Elastomers by Gas Decompression. *Rubber Chem. Technol.* **1995**, *68*, 197−211.
(8) Wijmans, J.; Baker, R. The Solution-Diffusion Model: a Review. *J. Membr. Sci.* **1995**, *107*, 1−21.
(9) Henry, W. Experiments on the Quantity of Gases Absorbed by Water, at Different Temperatures, and under Different Pressures. *Philos. Trans. R. Soc. London* **1803**, *93*, 29−276.
(10) Roff, W. J.; Scott, J. R. *Fibres, Films, Plastics and Rubbers: A Handbook of Common Polymers*; Elsevier, 2013.
(11) Ho, E. *Elastomeric Seals for Rapid Gas Decompression Applications in High-Pressure Services*; Research Report 485; Health and Safety Executive, 2006.
(12) Van Amerongen, G. J. The Permeability of Different Rubbers to Gases and Its Relation to Diffusivity and Solubility. *J. Appl. Phys.* **1946**, *17*, 972−985.
(13) Van Amerongen, G. J. Influence of Structure of Elastomers on Their Permeability to Gases. *J. Polym. Sci.* **1950**, *5*, 307−332.
(14) Müller-Plathe, F. Permeation of Polymers - A Computational Approach. *Acta Polym.* **1994**, *45*, 259−293.
(15) Widom, B. Some Topics in the Theory of Fluids. *J. Chem. Phys.* **1963**, *39*, 2808.
(16) Deitrick, G.; Scriven, L.; Davis, H. Efficient Molecular Simulation of Chemical Potentials. *J. Chem. Phys.* **1989**, *90*, 2370−2385.
(17) Jedlovszky, P.; Mezei, M. Calculation of the Free Energy Profile of H_2O, O_2, CO, CO_2, NO, and $CHCl_3$ in a Lipid Bilayer with a Cavity Insertion Variant of the Widom Method. *J. Am. Chem. Soc.* **2000**, *122*, 5125−5131.
(18) Kucukpinar, E.; Doruker, P. Molecular Simulations of Gas Transport in Nitrile Rubber and Styrene Butadiene Rubber. *Polymer* **2006**, *47*, 7835−7845.
(19) Sun, H.; Ren, P.; Fried, J. The COMPASS Force Field: Parameterization and Validation for Phosphazenes. *Comput. Theor. Polym. Sci.* **1998**, *8*, 229−246.
(20) Elber, R.; Karplus, M. Enhanced Sampling in Molecular Dynamics: Use of the Time- Dependent Hartree Approximation for a Simulation of Carbon Monoxide Diffusion Through Myoglobin. *J. Am. Chem. Soc.* **1990**, *112*, 9161−9175.
(21) Müller-Plathe, F.; Rogers, S. C.; van Gunsteren, W. F. Computational Evidence for Anomalous Diffusion of Small Molecules in Amorphous Polymers. *Chem. Phys. Lett.* **1992**, *199*, 237−243.
(22) Sok, R. M.; Berendsen, H. J. C.; van Gunsteren, W. F. Molecular Dynamics Simulation of the Transport of Small Molecules Across a Polymer Membrane. *J. Chem. Phys.* **1992**, *96*, 4699.
(23) Brandrup, J.; Immergut, E. H.; Grulke, E. A.; Abe, A.; Bloch, D. R. *Polymer Handbook*; Wiley: New York, 1989; Vol. *7*.
(24) Molinari, N.; Khawaja, M.; Sutton, A. P.; Mostofi, A. A. Molecular Model for HNBR With Tunable Cross-Link Density. *J. Phys. Chem. B* **2016**, *120*, 12700.
(25) Mackey, D.; Jorgensen, A. H. *Kirk-Othmer Encyclopedia of Chemical Technology*; John Wiley & Sons, Inc., 2000.
(26) Theodorou, D. N.; Suter, U. W. Detailed Molecular Structure of a Vinyl Polymer Glass. *Macromolecules* **1985**, *18*, 1467−1478.
(27) Plimpton, S. Fast Parallel Algorithms for Short-Range Molecular Dynamics. *J. Comput. Phys.* **1995**, *117*, 1−19.
(28) Jorgensen, W. L.; Maxwell, D. S.; Tirado-Rives, J. Development and Testing of the OPLS All-Atom Force Field on Conformational Energetics and Properties of Organic Liquids. *J. Am. Chem. Soc.* **1996**, *118*, 11225−11236.
(29) Bitzek, E.; Koskinen, P.; Gähler, F.; Moseler, M.; Gumbsch, P. Structural Relaxation Made Simple. *Phys. Rev. Lett.* **2006**, *97*, No. 170201.
(30) Nosé, S. A. Unified Formulation of the Constant Temperature Molecular Dynamics Methods. *J. Chem. Phys.* **1984**, *81*, 511−519.
(31) Ryckaert, J.-P.; Ciccotti, G.; Berendsen, H. J. Numerical Integration of the Cartesian Equations of Motion of a System with Constraints: Molecular Dynamics of n-Alkanes. *J. Comput. Phys.* **1977**, *23*, 327−341.
(32) Pronk, S.; Páll, S.; Schulz, R.; Larsson, P.; Bjelkmar, P.; Apostolov, R.; Shirts, M. R.; Smith, J. C.; Kasson, P. M.; van der Spoel, D.; et al. GROMACS 4.5: A High-Throughput and Highly Parallel Open Source Molecular Simulation Toolkit. *Bioinformatics* **2013**, *29*, 845−854. version 5.0.2
(33) Berendsen, H. J.; Postma, J. P.; van Gunsteren, W. F.; Hermans, J. *Intermolecular Forces*; Springer, 1981; pp 331−342.
(34) Harris, J. G.; Yung, K. H. Carbon Dioxide's Liquid-Vapor Coexistence Curve and Critical Properties as Predicted by a Simple Molecular Model. *J. Phys. Chem.* **1995**, *99*, 12021−12024.
(35) Shing, K. S.; Chung, S. T. Computer Simulation Methods for the Calculation of Solubility in Supercritical Extraction Systems. *J. Phys. Chem.* **1987**, *91*, 1674−1681.
(36) Rycroft, C. H.; Grest, G. S.; Landry, J. W.; Bazant, M. Z. Analysis of Granular Flow in a Pebble-Bed Nuclear Reactor. *Phys. Rev. E* **2006**, *74*, No. 021306.
(37) Politis, D. N.; Romano, J. P.; Wolf, M. *Subsampling*; Springer, 1999.
(38) Kleiner, A.; Talwalkar, A.; Sarkar, P.; Jordan, M. The Big Data Bootstrap. 2012, arXiv:1206.6415. arXiv.org e-Print archive. http://arxiv.org/abs/1206.6415.
(39) Efron, B.; Tibshirani, R. J. *An Introduction to the Bootstrap*; CRC Press, 1994.
(40) Klingender, R. C. *Handbook of Specialty Elastomers*; CRC Press, 2008.
(41) Figshare - Supporting Information. https://dx.doi.org/10.6084/m9.figshare.3556404.v1.

DOI: 10.1021/acs.jpcb.6b09690
J. Phys. Chem. B 2017, 121, 287−297